A&A 439, 1075–1091 (2005)
DOI: 10.1051/0004-6361:20042396

Astronomy & Astrophysics

Full computation of massive AGB evolution

II. The role of mass loss and cross-sections

P. Ventura and F. D'Antona

Osservatorio Astronomico di Roma, via Frascati 33, 00040 Monte Porzio Catone, Italy
e-mail: [ventura;dantona]@mporzio.astro.it

Received 19 November 2004 / Accepted 26 April 2005

Abstract. In the course of a systematic exploration of the uncertainties associated with the input micro- and macro-physics in the modeling of the evolution of intermediate mass stars during their Asymptotic Giant Branch (AGB) phase, we focus on the role of the nuclear reactions rates and mass loss. We consider masses $3 \leq M/M_{\odot} \leq 6.5$ for a metallicity typical for globular clusters, $Z = 0.001$, and compare the results obtained by computing the full nucleosynthesis with hot bottom burning (HBB), for a network of 30 elements, using either the NACRE or the Cameron & Fowler (CF88) cross-sections. The results differ in particular with respect to the ^{23}Na nucleosynthesis (which is more efficient in the NACRE case) and the magnesium isotopes ratios. For both choices, however, the CNO nucleosynthesis shows that the C+N+O is constant within a factor of two, in our models employing a very efficient convection treatment. Different mass loss rates alter the physical conditions for HBB and the length of the AGB phase, indirectly changing the chemical yields. These computations show that the predictive power of our AGB models is undermined by these uncertainties. In particular, it appears at the moment very difficult to strongly accept or dismiss that these sources play a key-role in the pollution of Globular Clusters (GCs), and that they have been the main stellar site responsible for the chemical anomalies that are observed at the surface of giant and turn-off stars of GCs, in the self-enrichment scenarios.

Key words. stars: evolution – stars: interiors – stars: AGB and post-AGB – stars: abundances

1. Introduction

Since the pioneering works by Schwarzschild & Harm (1965, 1967), and Iben (1975, 1976), it is now well known that intermediate mass stars (i.e. stars with initial masses $1 \leq M/M_{\odot} \leq 8$, hereinafter IMS) soon after the exhaustion of central helium experience a phase of thermal pulses (TPs), during which a CNO burning shell supplies for most of the time the global nuclear energy release; periodically, a He-burning shell is activated in thermally unstable conditions, triggering an expansion of all the outer layers, with the consequent extinction of CNO burning (Lattanzio & Karakas 2001). During the AGB evolution these stars suffer a strong mass loss, which ultimately peels off all the envelope mass, leaving a carbon-oxygen compact remnant which evolves as a white dwarf. The base of the external convective zone of the most massive IMS may become so hot ($T_{\rm bce} \geq 30 \times 10^6$ K) so as to favor an intense nucleosynthesis (hot bottom burning, HBB), whose results can be directly seen at the surface of the star due to the rapidity of convective motion (e.g. Ventura et al. 2002).

The ejecta of these stars might thus pollute the surrounding medium with material which was at least partially nuclearly processed: this is the reason why this class of objects has been invoked as a possible explanation for the chemical anomalies observed at the surface of giants and turn-off globular clusters stars (see e.g. Gratton et al. 2004), in what is commonly known as the self-enrichment scenario. An early generation of IMS evolved within the first ∼100−200 Myr of the cluster life, contaminated the interstellar-medium with gas which would be already nuclearly processed; this gas might have favored the formation of a later generation of stars, which would then show the observed chemical anomalies (Cottrell & Da Costa 1981; D'Antona et al. 1983; Ventura et al. 2001, 2002).

While there is a general agreement that the solution of this problem may be looked for in early AGB pollution, (Gratton et al. 2004), the quantitative agreement between the models and the abundance patterns shown by GC stars is not good (Denissenkov & Herwig 2003; Denissenkov & Weiss 2004). On the other hand, the AGB evolution of these stars is found to be strongly dependent on the convective model which is used to find out the temperature gradient within the external convective zone (Renzini & Voli 1981; Blöcker & Schonberner 1991; Sackmann & Boothroyd 1991; D'Antona & Mazzitelli 1996; Ventura & D'Antona 2005, hereinafter Paper I). The chemical content of their ejecta, in particular for some key-elements that are anticorrelated like oxygen and sodium and magnesium and aluminum, is strongly dependent not only on convection,

but also on the assumed mass loss rate and on the nuclear reaction rates. At the moment these uncertainties seriously undermine the predictive power of AGB models, and thus limit the predictions that can be made concerning their role within the framework of the self-enrichment scenario.

We investigate the AGB evolution of initial masses $3 \leq M/M_{\odot} \leq 6.5$, and focus our attention on their main physical properties, and on the chemical content of their ejecta. In Paper I we explored the dependence of the results on the convective model. In this work we complete the exploration by investigating the sensitivity of the results on: 1) the nuclear cross sections: we compare two sets of models calculated by assuming the Angulo et al. (1999) NACRE cross sections and those by Caughlan & Fowler (1988, hereinafter CF88); 2) the mass loss rate.

2. The evolutionary code

The stellar evolutions discussed in this paper were calculated by the code ATON2.1, a full description of which can be found in Ventura et al. (1998) (ATON2.0 version). The latest updates of the code, concerning the nuclear network, are given in Paper I. The interested reader may find in these papers a detailed description of the numerical structure of the code, and of the macro and micro-physics used to simulate the stellar evolutions.

2.1. Convection

The code allows us to calculate the temperature gradient within instability regions either by adopting the traditional MLT (Vitense 1953; Böhm-Vitense 1958), or the FST model (Canuto & Mazzitelli 1991; Canuto et al. 1996) for turbulent convection. The interested reader may find in Canuto & Mazzitelli (1991) a detailed description of the physical differences between the two models.

As we shall see, during the AGB evolution a non negligible fraction of the global nuclear release is generated within the convective envelope, therefore it is mandatory to adopt a diffusive approach, treating simultaneously mixing and nuclear burning. We therefore solve for each element the diffusion equation (Cloutman & Eoll 1976):

$$\left(\frac{\mathrm{d}X_i}{\mathrm{d}t}\right) = \left(\frac{\partial X_i}{\partial t}\right)_{\mathrm{nucl}} + \frac{\partial}{\partial m_{\mathrm{r}}}\left[(4\pi r^2\rho)^2 D \frac{\partial X_i}{\partial m_{\mathrm{r}}}\right] \quad (1)$$

stating mass conservation of element i. The diffusion coefficient D is taken as $D = \frac{1}{3}ul$, where u is the convective velocity and l is the convective scale length. We allow velocity to decay exponentially starting from the formal convective boundaries as:

$$u = u_{\mathrm{b}} \exp \pm \left(\frac{1}{\zeta f_{\mathrm{thick}}} \ln \frac{P}{P_{\mathrm{b}}}\right) \quad (2)$$

where u_{b} and P_{b} are, respectively, turbulent velocity and pressure at the convective boundary, P is the local pressure, ζ a free parameter connected with the e-folding distance of the decay, and f_{thick} is the thickness of the convective regions in fractions of H_{p}.

A detailed description of the treatment of convective velocities in the proximity of the formal borders of the convective zones (fixed by the Schwarzschild criteria) can be found in Sect. 2.2 of Ventura et al. (1998). In the same paper (Sect. 4.2) there is also an extensive discussion on the extra mixing determined by the use of a non-zero ζ.

The models presented in this paper adopt the FST convection, and the parameter ζ is fixed at $\zeta = 0.02$. No extra-mixing has been assumed from the base of the convective envelope: therefore the extension of the various dredge-up episodes, and the consequent changes of the surface chemical composition, must be considered as lower limits.

2.2. Nuclear network

The nuclear network includes 30 chemical species up to ^{31}P and 64 nuclear reactions. The list of all the reactions included in the nuclear network can be found in Paper I. The relevant cross-sections are taken either from Caughlan & Fowler (1988, CF88) or from Angulo et al. (1999, NACRE). In the range of temperatures of interest here ($7.5 \leq \log(T) \leq 8.2$, which are the typical values at the base of the external convective zone of massive AGBs) the largest differences between the two sets of cross-sections are the following:

- ^{17}O destruction by proton fusion is achieved much more easily in the NACRE case; also, contrary to CF88, the reaction ^{17}O(p,α)^{14}N is favored with respect to ^{17}O(p,γ)^{18}F.
- The cross-sections of the reaction ^{22}Ne(p,γ)^{23}Na are larger by ~3 orders of magnitude in the NACRE case, which makes sodium production much easier. As for sodium burning by proton fusion, the channel leading to the formation of ^{24}Mg is favored in the NACRE case.

2.3. Mass loss

The mass loss rate is calculated according to Blöcker (1995), who modifies the Reimer's formula in order to simulate the strong mass loss suffered by these stars as they climb along the AGB. The complete expression is:

$$\dot{M} = 4.83 \times 10^{-9} M^{-2.1} L^{2.7} \dot{M}_{\mathrm{R}} \quad (3)$$

where $\dot{M}_{\mathrm{R}} = 10^{-13}\eta_{\mathrm{R}} LR/M$ is the canonical Reimer's rate, and η_{R} is a free parameter directly connected to the mass loss rate.

$\dot{M}$ was described according to Eq. (3), with the parameter $\eta_{\mathrm{R}} = 0.02$ for the "standard" case; we then consider evolutions with $\eta_{\mathrm{R}} = 0.1$ and $\eta_{\mathrm{R}} = 0.2$. In all cases mass loss was applied for all the evolutionary phases.

2.4. Model inputs

We evolved models with initial masses $3\ M_{\odot} \leq M \leq 6.5\ M_{\odot}$ starting from the pre-main sequence along the whole TP phase. Above the upper mass limit, models ignite carbon in the center, skipping the AGB phase. Below the lower limit models do not achieve HBB conditions.

When the envelope mass becomes "small" ($M_e < 1\ M_\odot$) a much higher temporal resolution is required, which renders the computations extremely time-consuming; since the chemical yields are almost unaffected by the following phases, we decided to stop the evolution when the mass of the envelope falls below $\sim 0.5\ M_\odot$.

We adopted an initial metallicity, Z, typical of those globular clusters (GCs) like NGC 6752, M 3, M 13, whose stars show the largest chemical anomalies, i.e. $Z = 0.001$ and $Y = 0.24$. For all the elements included in our network, we adopted solar-scaled initial abundances. This is to be taken into account if we want to compare the results with observations, as the starting initial mass fractions of abundant elements play a role in the determination of the final yield. e.g., as [O/Fe] $\sim +0.3$ in population II stars, this initial abundance will be reflected in the evolution with oxygen depletion. Numerical tests show that the results for oxygen may be roughly scaled up by the initial enhancement with respect to the solar scaled value. For instance, if the solar scaled model produces a yield with [O/Fe] $= -0.5$, the yield starting from initial [O/Fe] $= +0.3$ would have been [O/Fe] $= -0.2$.

3. NACRE results

3.1. The pre-AGB phase

Table 1 summarizes the main physical properties of our models, related to the evolutionary phases preliminary to the AGB evolution. During the main sequence phase the models develop a central convective region which progressively shrinks in mass, with a maximum extension ranging from $\sim 0.72\ M_\odot$ for the $3\ M_\odot$ model up to $\sim 2\ M_\odot$ for the $6.5\ M_\odot$ model.

The total duration of the H-burning phase (t(H)) is a decreasing function of mass: the less massive model, with initial mass $M = 3\ M_\odot$, consumes central hydrogen in $\sim$275 Myr, while the $6.5\ M_\odot$ model keeps burning hydrogen for 54 Myr (Fig. 1, top panel).

During the first dredge-up, following H-exhaustion, the convective envelope reaches stellar layers which were previously touched by CNO burning via the CN cycle, with the conversion of some ^{12}C to ^{14}N: consequently, the surface ^{14}N is increased by a factor of $\sim$2, while ^{12}C decreases from the initial value of $X(^{12}\mathrm{C}) = 1.73 \times 10^{-4}$ to $X(^{12}\mathrm{C}) = 1.3 \times 10^{-4}$. The lithium surface abundance drops by a factor of $\sim$50, because surface lithium is mixed within an extended region where lithium was previously destroyed via proton fusion; this drop is dependent on the stellar mass, and a spread of a factor of $\sim$2 is found among the models.

During the following phase of core helium burning a convective core is formed, again with a dimension increasing with mass: it is $\sim 0.28\ M_\odot$ for the $3\ M_\odot$ model, while it is $\sim 0.7\ M_\odot$ for the $6.5\ M_\odot$ model (see the 5th column of Table 1). We see from Fig. 1 (bottom panel) that the ratio between the He-burning (t(He)) and the MS times is decreasing with mass, ranging from $\sim$20% to slightly higher than 10% for the $6.5\ M_\odot$ model. Once helium is burnt-out in the stellar core, 3α reactions carry on in an intermediate layer, triggering a general expansion of the structure, which eventually extinguishes the CNO burning shell. The general cooling of the star favors the formation of a very deep and extended external convective zone, in what is commonly known as the second dredge-up episode.

From the top panel of Fig. 2 we see that the mass coordinate corresponding to the maximum penetration of the outer envelope is slightly increasing with mass, with a difference of $\sim 0.2\ M_\odot$ between the 3 and $6.5\ M_\odot$ models. The most interesting quantity is however shown in the bottom panel of the same figure, where we report the variation as a function of the initial mass of $\delta M = M_{\rm CNO} - M_{\rm min}$, where $M_{\rm CNO}$ and $M_{\rm min}$ are, respectively, the location of the CNO burning shell immediately before the second dredge-up, and the minimum point

Table 1. Physical properties of the NACRE models.

M	t(H)[a]	$M^b_{\rm c,H}$	t(He)[a]	$M^c_{\rm c,He}$	$M^d_{\rm 1dup}$	$M^e_{\rm 2dup}$	$\delta(M_{\rm 2dup})^f$
3.0	276	0.72	56	0.28	0.85	0.78	0.01
3.5	195	0.93	33	0.32	1.19	0.84	0.05
4.0	145	1.04	23	0.36	1.50	0.87	0.15
4.5	112	1.21	16	0.44	1.86	0.90	0.26
5.0	90	1.40	12	0.48	2.10	0.93	0.37
5.5	75	1.57	10	0.57	2.42	0.97	0.48
6.0	63	1.85	7.6	0.62	2.70	1.00	0.58
6.5	54	2.05	6.3	0.70	2.85	1.05	0.68

[a] Times are expressed in Myr.
[b] Maximum extension (in $M_\odot$) of the convective core during H-burning.
[c] Maximum extension (in $M_\odot$) of the convective core during He-burning.
[d] Mass coordinate (in $M_\odot$) of the innermost layer reached during the first dredge-up.
[e] Mass coordinate (in $M_\odot$) of the innermost layer reached during the second dredge-up.
[f] Amount (in $M_\odot$) of dredged-up material nuclearly processed by CNO burning.

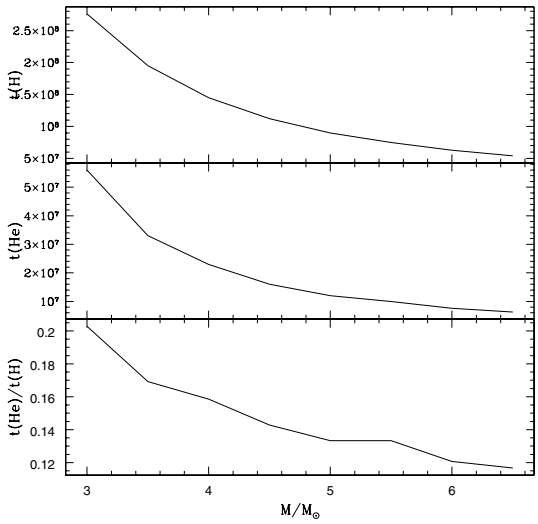

Fig. 1. The duration of the phases of hydrogen and helium burning as a function of the initial mass for the NACRE intermediate mass models. *Top*: H-burning time; *middle*: He-burning time; *bottom*: ratio between the He-burning and the H-burning times.

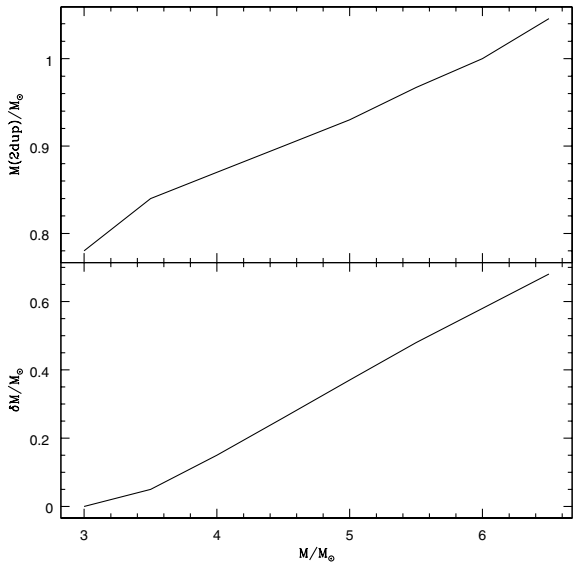

Fig. 2. *Top*: the mass coordinate of the innermost point reached by the base of the envelope during the second dredge-up for the same models discussed in Fig. 1. *Bottom*: the penetration (in solar masses) of the base of the external convective zone beyond the location of the CNO burning shell during the second dredge-up.

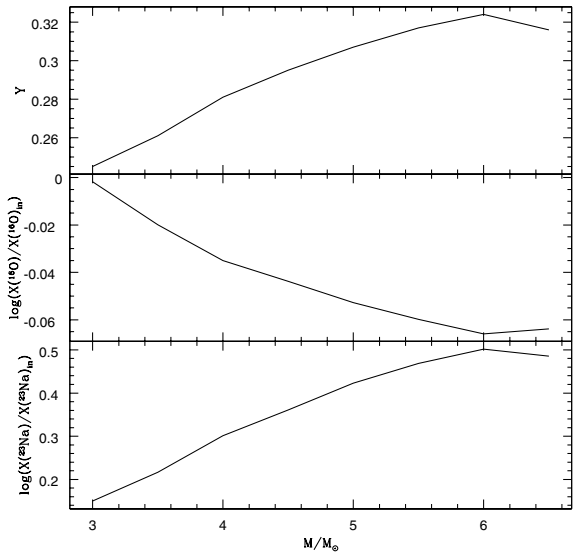

Fig. 3. The variation of the surface chemical abundances of some elements following the 2nd dredge-up. *Top*: helium mass fraction; *middle*: variation of the ^{16}O abundance, expressed as the logarithm of ratio between the final abundance and the initial mass fraction; *bottom*: the same as the middle panel, but for ^{23}Na.

(in mass) reached by the base of the outer convective zone. δM is therefore a measure of the amount of processed material which is carried to the surface during the second dredge-up. We see that a poor mixing is expected in the 3 $M_\odot$ model, while in the 6.5 $M_\odot$ case ∼0.7 $M_\odot$ of CNO processed material is mixed with the surface layers. During the second dredge-up the surface ^{14}N is increased by another factor of ∼2, the carbon abundance decreases to $X(^{12}\mathrm{C}) \sim 1.15 \times 10^{-4}$, while lithium is not dramatically affected, because the surface lithium abundance was already heavily lowered during the first dredge-up. At the second dredge-up, the helium, sodium and oxygen abundances are changed (depending on the stellar mass), as can be seen in the three panels of Fig. 3. This can be understood on the basis of the following considerations:

- The amount of mixed material during the second dredge-up sensibly increases with the stellar mass (see Fig. 2).
- During the second dredge-up the base of the outer envelope reaches layers which were previously touched by full CNO burning, thus explaining the oxygen reduction.
- The amount of material previously touched by CNO burning and mixed to the surface is larger than in the first dredge-up case, thus the increase of the surface helium abundance is very large, especially in the most massive models.

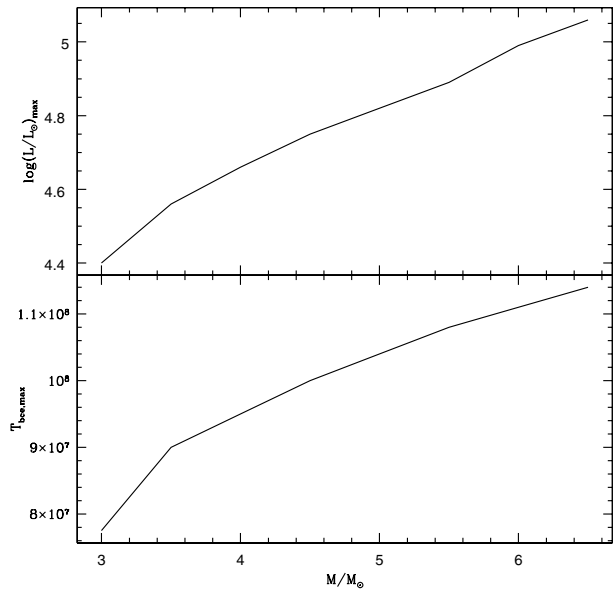

Fig. 4. The maximum luminosity (*top*) and temperature at the base of the convective envelope (*bottom*) achieved by the standard NACRE models during their AGB evolution.

3.2. The AGB phase

For most of the AGB evolution the global nuclear energy release is generated within a CNO burning shell, which may also overlap, in some cases, with the external convective zone. As hydrogen is consumed, the core mass increases, and the CNO burning takes place at higher temperatures, thus favoring an increase of the stellar luminosity. This is halted by mass loss, which progressively reduces the mass of the envelope, and eventually leads to a general cooling of the outer stellar layers. The base of the convective zone becomes cooler and cooler in the latest evolutionary stages; when the mass of the envelope drops below ∼1 $M_\odot$ the temperatures within the whole external zone become so small to prevent any further nucleosynthesis. For each model, we may therefore find out maximum values of both luminosity and $T_{\rm bce}$, which we report as a function of the initial mass of the star in the two panels of Fig. 4. We see that even the least massive of our models, i.e. the 3 $M_\odot$ model,

Table 2. Chemical content of the ejecta of the NACRE models.

$M_{\rm ZAMS}$	Y^a	$\log(\epsilon(^7{\rm Li}))^b$	$[^{12}{\rm C}]^c$	$[^{14}{\rm N}]$	$[^{16}{\rm O}]$	$({\rm C+N+O})^d$	$[^{23}{\rm Na}]$	$[^{24}{\rm Mg}]$	$[^{25}{\rm Mg}]$	$[^{26}{\rm Mg}]$	$^{25}{\rm Mg}/^{24}{\rm Mg}$	$^{26}{\rm Mg}/^{24}{\rm Mg}$
3.0	0.26	2.41	−0.10	1.52	0.01	3.24	1.21	0.03	0.22	0.56	0.20	0.50
3.5	0.27	2.20	−0.44	1.37	−0.19	2.18	0.75	−0.01	0.37	0.40	0.31	0.39
4.0	0.29	2.06	−0.56	1.28	−0.39	1.70	0.46	−0.28	0.60	0.41	0.98	0.73
4.5	0.32	1.96	−0.60	1.24	−0.49	1.51	0.02	−0.66	0.60	0.38	2.37	1.63
5.0	0.32	1.91	−0.70	1.13	−0.61	1.17	−0.16	−0.95	0.50	0.35	3.68	3.00
5.5	0.32	1.94	−0.80	1.04	−0.59	0.99	−0.37	−1.13	0.53	0.31	6.13	4.18
6.0	0.32	1.91	−0.82	1.01	−0.54	0.96	−0.43	−1.23	0.60	0.28	8.96	4.96
6.5	0.32	2.25	−0.81	1.01	−0.46	1.00	−0.37	−1.27	0.66	0.25	11.34	5.02

[a] Helium mass fraction.
[b] $\log(\epsilon(^7{\rm Li})) = \log(^7{\rm Li/H}) + 12.00$.
[c] $[A] = \log(X(A)_{\rm ej}) - \log(X(A)_{\rm in})$.
[d] Ratio between the average (C+N+O) abundance of the ejecta and the initial (C+N+O) value.

achieves at the base of the external convective zone temperatures so large ($T_{\rm bce} \sim 7.75 \times 10^7$ K) to trigger HBB.

In all the models, shortly after the beginning of the TPs phase, the TDU operates following each TP, changing the surface chemistry. The efficiency λ of the TDU increases with the evolution, and is higher in the less massive models. We find that for $M \geq 5\ M_\odot$ a maximum value of $\lambda \sim 0.4$ is attained in the latest evolutionary stages, while a significantly larger value of $\lambda \sim 0.7-0.8$ is reached along the evolutions of the models with masses 3−3.5 $M_\odot$.

The chemical composition of the ejecta of our NACRE models, calculated over the lifetime of the star, is summarized in Table 2. With the only exception of lithium, for the other elements we indicate the logarithm of the ratio between the average chemical abundance of the ejecta and the initial value. Therefore, a value of 0 indicates that the chemical content of the ejecta is the same as the initial chemistry.

3.3. The CNO elements

In the three panels of Fig. 5 we show the variation during the AGB evolution (including also the changes due to the second dredge-up) of the surface abundances of the CNO elements; we chose the stellar mass as abscissa in order to have an idea of the average chemical content of the ejecta of these stars. We see (left-lower panel) that oxygen is depleted in all cases apart from the 3 $M_\odot$ model, the heaviest depletion being for the largest masses, in agreement with the physical situation present at the base of the external convective zone. We note the apparently anomalous behavior of the 6 and 6.5 $M_\odot$ models, which have a flatter declining profile of the surface oxygen with mass: this can be understood on the basis of the fact that these latter models are already extremely luminous during the pre-AGB phase, so that a large fraction of the mass is lost when the oxygen abundance is still close to the value left behind by the second dredge-up.

In the right panel we may follow the evolution of the surface abundance of carbon: we note an early phase of destruction in all models, which corresponds to the stage when only the CN cycle is active, followed by a later increase, when the full CNO cycle is activated; in the less massive models we recognize the signature of an efficient third dredge-up.

Even in this case we note the peculiar behavior of the 3 $M_\odot$ model, in which the 3rd dredge-up is highly efficient since the first TPs, so that the surface ^{12}C abundance increases up to $\log(X(^{12}{\rm C})) \sim -3.4$; only in a later time, ∼200 000 yr after the beginning of the AGB phase, when ∼0.5 $M_\odot$ have been lost, HBB occurs, and the ^{12}C abundance starts to decrease. The 3rd dredge-up after 10 TPs is so efficient that also some ^{16}O is carried outwards; ^{16}O reaches a maximum abundance after 15 TPs and then decreases approximately to the initial value: this is the only model for which we find an oxygen content of the ejected material that is larger than the original composition (see the 6th column of Table 2 and the top panel of Fig. 9). The combination of the effects of HBB and of the almost constant surface abundance of ^{16}O prevents the formation of a carbon star. From this discussion we argue that 3 $M_\odot$ is approximately the lower limit for models achieving HBB with the full CNO cycle operating during the AGB evolution. No ^{16}O depletion can be achieved in less massive models.

The carbon, nitrogen and oxygen abundance of the ejecta are reported in Cols. 4−6 of Table 2. We see that the carbon content of the expelled material is always smaller than the initial value, due to the drop of the surface carbon which follows the first and especially the second dredge-up. The depletion factor is lower the lower is the mass, because in the less massive models more carbon is produced later in the AGB evolution by the 3rd dredge-up. We note that even for the 3 $M_\odot$ model, despite the early phase of ^{12}C production at the beginning of the TPs phase (see the right panel of Fig. 5), we find a negative $[^{12}{\rm C}]$, due to a later phase of ^{12}C depletion at the base of the convective envelope via proton fusion.

From Col. 5 of Table 2 we see that the nitrogen abundance of the ejecta is always at least a factor of ∼10 larger than the initial value. Nitrogen is mixed to the surface through the first and second dredge-up, then its surface abundance increases due to HBB, via CN and ON cycling, and may further increase following each third dredge-up episode, via the conversion of additional primary ^{12}C mixed into the envelope. Also in this case, the reason for the larger ^{14}N abundances found in the ejecta of

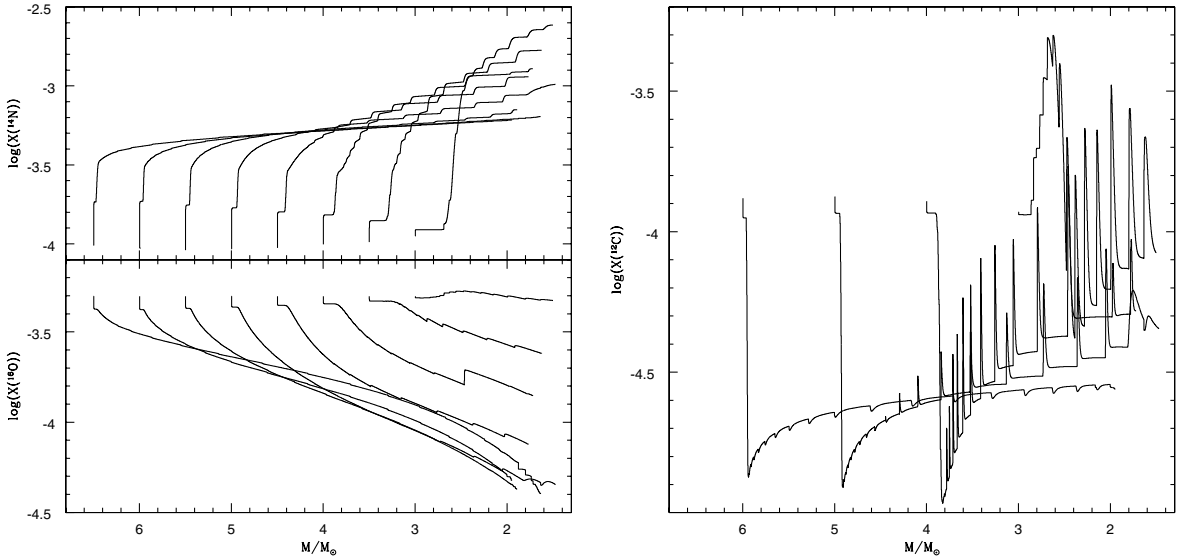

Fig. 5. Variation of the surface chemical abundances of the CNO elements during the evolution of the same models as in Fig. 1. For clarity reason, for ^{12}C we decided to show only the variation at the surface of the models with initial masses 3, 4, 5 and 6 $M_{\odot}$.

the less massive models is the higher number of TPs and the larger efficiency of 3rd dredge-up episodes.

As for oxygen, with the only exception of the 3 $M_{\odot}$ model we find, in agreement with what is shown in the left-lower panel of Fig. 5, $[^{16}\mathrm{O}] < 0$ in all cases (see also the top panel of Fig. 9). We note that the minimum value of $[^{16}\mathrm{O}]$, i.e. $[^{16}\mathrm{O}] = -0.61$, is reached for $M = 5\ M_{\odot}$, because the yield of more massive models is influenced by the very strong mass loss already efficient at the 2nd dredge-up, when no HBB had started yet.

The oxygen isotopes show a similar behavior in all our models. The surface abundance of ^{17}O is increased during the second dredge-up by ∼0.2 dex; at the very beginning of the AGB evolution ^{17}O is produced at the base of the external zone due to partial ^{16}O burning, so that, particularly in the most massive models, its abundance is increased by a factor of ∼10. Later on, when ^{16}O burning is more efficient, the surface ^{17}O abundance reaches an equilibrium value, and then decreases as the ^{16}O. The maximum surface ^{17}O abundance is $\log[X(^{17}\mathrm{O})] \sim -5.5$ for the model with initial mass 6.5 $M_{\odot}$, while it is $\log[X(^{17}\mathrm{O})] \sim -5.8$ for the 3 $M_{\odot}$ model. The ^{18}O abundance is dramatically decreased during the second dredge-up, passing from $\log[X(^{18}\mathrm{O})] \sim -6$ to $\log[X(^{18}\mathrm{O})] \sim -10$. At the beginning of the TPs phase some ^{18}O is produced via proton capture by ^{17}O, so that its abundance rises up by 2 orders of magnitude for the 6.5 $M_{\odot}$ model (and by one order of magnitude in the 3.5 $M_{\odot}$ model). Like ^{17}O, a maximum value is reached, after which the surface ^{18}O abundance decreases as ^{16}O is consumed within the envelope.

An important outcome of most of our models is that the global C+N+O abundance of the ejecta is constant within a factor of ∼2. This can be seen in the 7th column of Table 2, where we report the ratio between the global CNO abundance of the ejecta and the initial value. With the only exception of the 3 $M_{\odot}$ model, for which the effects of the 3rd dredge-up overwhelm those of HBB, the values of the ratio between the average (C+N+O) abundance of the ejecta and the initial value are always ≤2, being close to 1 for the most massive models.

These results are at odds with recent computations of AGB models of the same metallicity by Fenner et al. (2004), where it was shown that:

- Only models more massive than 6 $M_{\odot}$ achieve surface oxygen depletion.
- The material expelled by AGBs is for all the computed masses both carbon and nitrogen rich.
- The C+N+O strongly increases with respect to the initial value.

These findings led the authors to conclude that massive AGBs hardly played a relevant role in the pollution of the interstellar medium of GCs, since spectroscopic analysis of NGC 6752 stars found an anti correlation between [C/Fe] and [N/Fe] independent of the luminosity (Grundahl et al. 2002); besides, the C+N+O sum is approximately constant in many CGs (Ivans et al. 1999). The different convective model adopted is the reason for the difference between our results and those obtained by Fenner et al. (2004) (see the detailed discussion in Paper I), the FST model leading much more easily to efficient HBB which, in turn, triggers larger luminosities, shorter AGB life-times, and a smaller number of 3rd dredge-up episodes.

3.4. Sodium nucleosynthesis

Figure 6 shows the behavior of surface sodium. In all cases we see an increase due to the second dredge-up, followed by an early phase of sodium production due to ^{22}Ne burning during the first TPs. Later on, when the whole Ne–Na cycle is active, the sodium abundance declines. For $M \leq 5\ M_{\odot}$ the third dredge-up favors a later phase of sodium production, via proton capture by ^{22}Ne mixed into the envelope. The ^{22}Ne itself is a result of two α captures on the ^{14}N mixed into the helium intershell at each third dredge up episode.

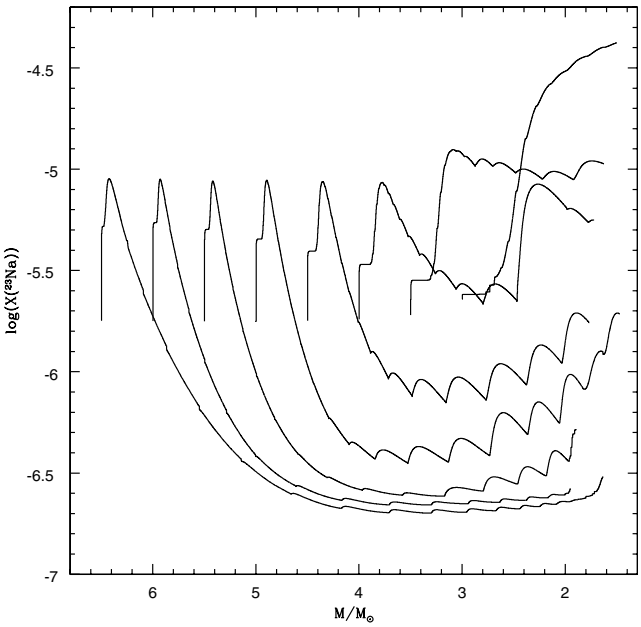

Fig. 6. The variation of the surface sodium abundance for the standard NACRE models.

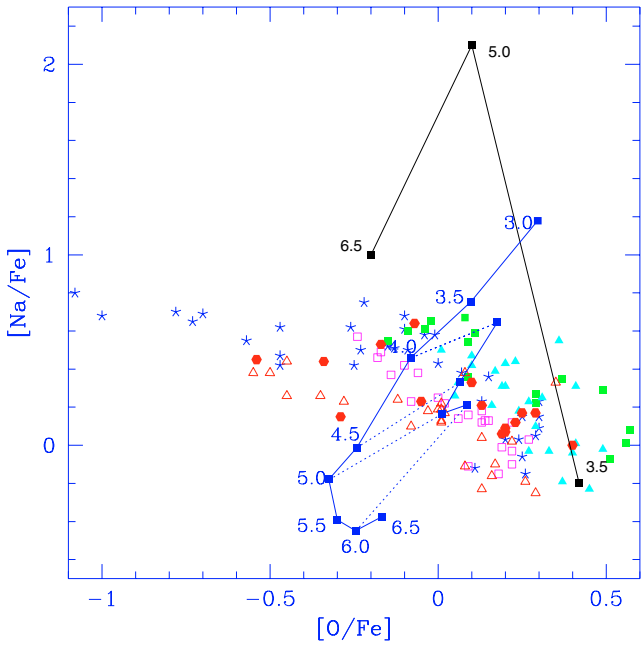

Fig. 7. Observed data which define the anticorrelation sodium vs. oxygen in the stars of several GCs. Stars: M 13, open squares: M 3 (both from Sneden et al. 2004); full squares: NGC 6752 from Grundahl et al. (2002); full triangles: M 4 and open triangles: M 5 (both from Ivans et al. 1999); full dots: NGC 2808 from Carretta et al. (2003). Models by Fenner et al. (2004) of 3.5, 5 and 6.5 $M_{\odot}$, and models of this paper are also shown. The standard models with $\eta = 0.02$ (left line, points labelled by the mass value) and the models with $\eta = 0.10$ have been shifted by 0.3 dex in [O/Fe] to be compared with the observations. Equal masses are joined.

Particularly in the models with masses $M \leq 4\ M_{\odot}$ a considerable amount of sodium is produced. In the 3 $M_{\odot}$ model, following each TP, sodium is produced by ^{22}Ne burning; during the quiescent CNO burning phases the bottom of the envelope is hot enough to activate the Ne–Na chain, but not to allow the Ne–Na reactions to act as a cycle (Arnould et al. 1999), which favors large production of sodium.

The bottom panel of Fig. 9 shows the average sodium abundance of the ejected material, as a function of the stellar initial mass. Sodium is produced within the less massive models due to the third dredge-up and to the modest sodium burning, but is destroyed within the massive models, so that the sodium content of the ejecta of these latter is under abundant with respect to the initial value. We see that only the models with initial masses clustering around 4 $M_{\odot}$ are able to expell material that is both sodium rich and oxygen poor, and so *only the abundances in these ejecta would be in agreement with the oxygen-sodium anti correlation* observed within GCs stars (Gratton et al. 2001; Sneden et al. 2004).

Also in regard to sodium, we note the different predictions of our models compared to those by Fenner et al. (2004), who expect extremely high sodium production for all the masses considered here. (see their Figs. 1 and 7). Within their models the sodium produced is primary, and is produced via ^{22}Ne burning, this latter being dredged-up from the inner helium layers. In principle, this mechanism could work also in our models (see Fig. 6), but sodium production is made much less efficient due to: *i)* the smaller number of 3rd dredge-up episodes; *ii)* the larger temperatures, which favor sodium destruction. We therefore see that again the treatment of convection is the main reason for the differences found in terms of the sodium content of the ejecta of AGBs. It is interesting to note that, in terms of the self-enrichment scenario, we have the opposite problem compared to the Fenner et al. (2004) models: they produce too much sodium, in great excess with the increase observed in some GCs stars (that is at most of ∼0.5 dex), while in our case, for the most massive models, we destroy it, as also predicted by Denissenkov & Weiss (2004).

Figure 7 compares our results with those by Fenner et al. (2004) in the plane of oxygen versus sodium abundances, in which we have reported several sets of observational data. Our results should be shifted by +0.3 dex in oxygen to be properly compared with the observations. We see that both sets are unable to reproduce the data.

3.5. The magnesium and aluminum isotopes

Figure 8 shows the variation of the magnesium and aluminum isotopes along the standard evolutions of 3.5, 4 and 5 $M_{\odot}$. As the rate of proton capture on this isotope increases with temperature at the bottom of the convective envelope, ^{24}Mg is more depleted for larger masses. Masses $M > 5\ M_{\odot}$ have qualitatively the same behavior, with more efficient ^{24}Mg destruction. The heaviest destruction is found within the 6.5 $M_{\odot}$ model, in which the surface final abundance is lower with respect to the initial value by a factor of ∼500. We see from Table 2 that the ^{24}Mg abundance of the ejecta is lower the larger the initial mass, reaching a minimum value of [^{24}Mg] ~ -1.3 for the 6.5 $M_{\odot}$ model. The abundance of ^{25}Mg, on the contrary,

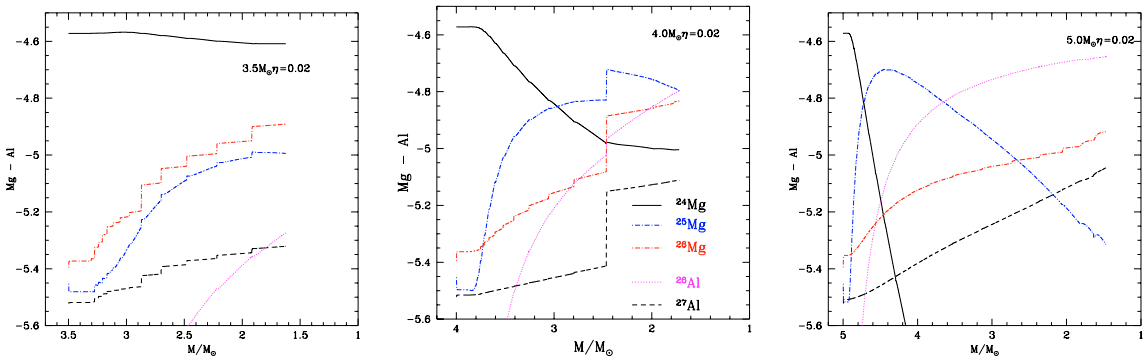

Fig. 8. The variation of the magnesium and aluminum isotopes for the standard NACRE models of 3.5, 4 and 5 $M_{\odot}$.

in a first stage increases due to the ^{24}Mg proton capture during the first TPs, and later on its abundance decreases (e.g. in the 5 $M_{\odot}$) due to burning to ^{26}Al. The ^{26}Al however decays into ^{26}Mg only on a timescale of 7×10^5 yr, and so this element is a bottleneck for further proton capture on ^{26}Mg, which leads to ^{27}Al. A direct path to ^{25}Mg and ^{26}Mg is through the third dredge up, as these isotopes are synthesized in the helium shell via capture of α on ^{22}Ne, and release respectively a neutron or a gamma ray. This production mechanism is evident in Fig. 8 for ^{26}Mg, while it is also clear (especially in the left figure, relative to the 3.5 $M_{\odot}$ evolution) that the production of ^{25}Mg is due to two mechanisms, dredge up and proton capture on ^{24}Mg. As we do not have a large number of thermal pulses, the ^{27}Al abundance can not rise by the huge factor (close to 10) shown by Globular Cluster stars (see Grundhal et al. 2002, for the giants of the cluster NGC 6752). Further, the ratios between the magnesium isotopes are not consistent with the results by Yong et al. (2003), which indicate that ^{25}Mg remains at 10% of the ^{24}Mg abundance, and ^{26}Mg reaches at most ~50%. The observational result both implies a not dramatic burning of ^{24}Mg, and a mild, if any, increase in ^{25}Mg and ^{26}Mg. Notice that, in addition, we have to count into the ^{26}Mg abundance also the abundance of the unstable isotope ^{26}Al, and the result is at variance with observations.

In spite of the not good agreement of these abundances with the observation, at least the trend of our models is in the right direction, as the ratios ^{25}Mg/^{24}Mg and ^{26}Mg/^{24}Mg do not exceed ~3 for masses up to 5 $M_{\odot}$. The corresponding models by Fenner et al. (2004), in which the smaller efficiency of convection allows a longer evolutionary phase and many episodes of third dredge up provide ratios larger than 100. Notice also that for elements whose abundances are very small, also the initial abundances and the exact modeling of the thermal pulses may influence strongly the results. The central part of Fig. 8 in fact shows that the evolution of the 4 $M_{\odot}$ suffers an anomalous episode of third dredge up, which we are uncertain whether to attribute to numerics or to a real effect. This lonely episode changes the surface abundances of sodium and magnesium in such a way that the resulting yields of the elements having low abundances are affected, although the most abundant yields (e.g. CNO) are not. This requires an additional detailed study before we can reject or accept these results as conclusive for the problem of abundance variations in GCs.

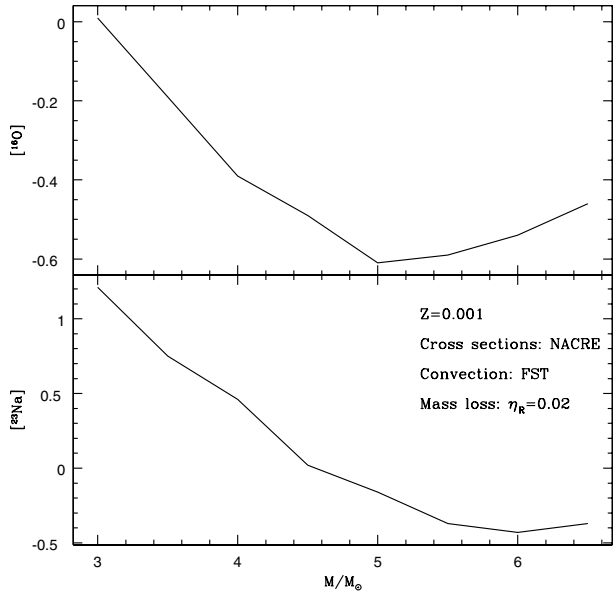

Fig. 9. The average chemical content of the ejecta of the standard NACRE models as a function of the initial mass. *Top*: oxygen abundance; *bottom*: sodium abundance.

3.6. The lithium content of the ejecta

We conclude this general description with lithium, which is created during the first TPs via the Cameron & Fowler (1971) mechanism, and then destroyed as soon as ^{3}He is extinguished in the envelope. We see from the 3rd column of Table 2 that the lithium content of the ejecta first decreases with increasing mass. In fact, the larger the mass, the hotter the base of the convective envelope, the more rapidly ^{3}He is destroyed, the shorter the phase during which the star shows up as lithium-rich; for models more massive than 5 $M_{\odot}$, as already discussed for the oxygen content of the ejecta, we have that the mass loss is so strong during the first TPs that a considerable fraction of the mass is lost when lithium has been produced and not yet destroyed. The differences among the lithium abundances of the various models is however within a factor of ~2, and is about a factor 2 smaller than the average abundance which is observed in population II stars.

3.7. The overall chemistry of the ejecta

In examining the overall chemical content of the ejecta of our models, there are four common features, which hold independently of mass:

1. The lithium content is within a factor 2 of the value observed in population II stars.
2. The ejecta are helium rich: particularly models with initial mass $M > 4\ M_{\odot}$ during the second dredge-up reach surface helium mass fractions of $Y \sim 0.32$. Helium is also produced during the AGB phase during any interpulse phase, but the consequent overall increase of Y is limited in all cases to $\delta Y \sim 0.005$.
3. When compared with the initial abundances, we see that the material lost during the evolutions is enhanced in ^{14}N by at least a factor of ∼10 and depleted in ^{12}C by a factor of ∼4. This trend is consistent with the observations, indicating CN cycled composition and no carbon enhancement (Cohen et al. 2002; Cohen & Melendez 2004). However, the anticorrelation between carbon and nitrogen is not found in the yields as a function of the initial mass (see Table 2).
4. The (C+N+O) abundance is constant within a factor of ∼2, due to the small number of 3rd dredge-up episodes.

For the other elements, the stellar yields depend sensibly on the stellar mass, both quantitatively and qualitatively. The more massive models pollute the interstellar medium with material that is oxygen and (partially) sodium depleted. ^{24}Mg is heavily depleted (a factor of ∼10 with respect to the initial value), so that high magnesium isotopic ratios (larger than solar) are expected.

Conversely, within models less massive than $\sim 4.5\ M_{\odot}$, the temperature at the base of the external zone is such that the Ne–Na cycle is only partially activated, and only in the last AGB phases; consequently, the ejecta of these stars are sodium rich and oxygen poor. The ^{24}Mg depletion is negligible due to the low temperatures, therefore the magnesium isotopic ratios are reduced, although not at the level that would provide agreement with the relevant observations by Yong et al. (2003). Further, the magnesium – aluminum anti correlation (see e.g. Grundahl et al. 2002) is not fully reproduced, as the ^{27}Al production is not very efficient.

4. NACRE vs. CF88

The nuclear cross-sections play a delicate role in determining the main physical and chemical properties of the AGB evolutions. From a physical point of view, a variation of the cross-sections of the nuclear reactions mostly contributing to the global energy release might influence the thermal stratification of the star; from a chemical point of view, a change in the cross-sections of those reactions involving key elements like sodium or magnesium, though energetically not relevant, might alter the equilibrium abundances, hence the average chemical content of the ejecta.

We explore the uncertainty of the results connected with the cross-sections of the various reactions included within our network by performing a detailed comparison between the results presented in the previous section and those obtained with the CF88 release, which are still widely used in modern AGB computations. This was made also to have an idea of the degree of uncertainty of the results connected with the cross-sections of the various reactions included within our network. We calculated a new set of models with the same physical and chemical inputs of the NACRE models, but adopting the CF88 rates for the nuclear cross-sections.

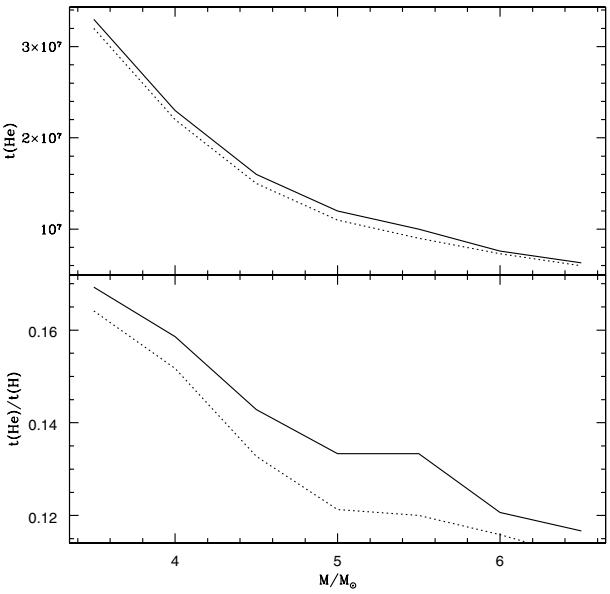

Fig. 10. The comparison between the time-scale for helium burning (*top*) and the ratio between the time-scales for helium and for hydrogen burning (*bottom*) for the NACRE (solid) and CF88 (dotted) models of intermediate mass.

We did not find any appreciable difference during the MS evolution for the whole range of masses involved, as the cross-sections of the relevant reactions are the same for both sets of models. For each value of the initial mass, we could verify that the duration of the H-burning phase, the innermost point reached during the first dredge-up and the consequent changes in the surface chemistry are unchanged.

The first differences between the models appear in the duration of the helium burning phase, as can be seen in Fig. 10. Also the ratio between the times of helium and hydrogen burning are consequently affected. The reason for this difference is the rate of the reaction $^{12}\mathrm{C} + \alpha \rightarrow {}^{16}\mathrm{O}$, which is larger by a factor of ∼1.7 in the NACRE case. This leads to slightly longer time-scales for helium burning (see the discussion in Imbriani et al. 2001; and Ventura & Castellani 2005).

The AGB evolution of the models is physically very similar, because the global nuclear energy release during the quiescent phase of CNO burning (which, we recall, is for most of the time the only nuclear source active within the star) is dominated by the proton captures by ^{12}C, ^{13}C and ^{14}N nuclei, whose corresponding cross-sections are similar in the two cases. We could verify that the duration of the whole AGB phase for the two sets of models, as well as the temporal evolution of the most relevant physical quantities, are essentially the same.

In the four panels of Fig. 11 we show the average chemical content of the ejecta, in terms of lithium and CNO

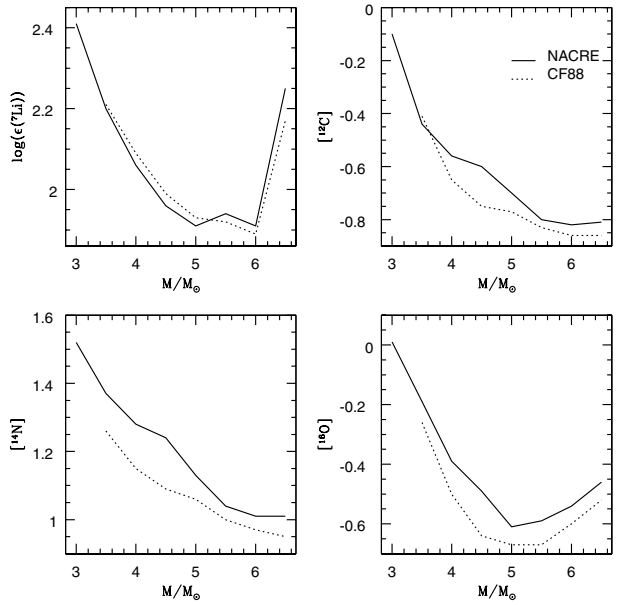

Fig. 11. The average chemical content of the ejecta of the NACRE (solid) and CF88 (dotted) models of intermediate mass in terms of lithium, carbon, nitrogen and oxygen abundances.

abundances. We see that the lithium content is extremely similar for the two sets of models, while the ^{12}C, ^{14}N and ^{16}O abundances are lower in the CF88 models, when compared to NACRE. This difference is due to the cross-sections of the reactions of proton capture by ^{17}O atoms, which, as already discussed in Sect. 2, are much lower in the CF88 case. The three left-panels of Fig. 12 show, respectively, the variation with temperature of the ratio (CF88/NACRE) between the rates of the reactions ^{17}O(p,γ)^{18}F (top panel), ^{17}O(p,α)^{14}N (middle panel), and of the ratio $\sigma(^{17}\mathrm{O(p,}\gamma)^{18}\mathrm{F})/\sigma(^{17}\mathrm{O(p,}\alpha)^{14}\mathrm{N})$ in the two cases. We can see that in the range of temperatures of interest here ($7.5 \leq \log T \leq 8$) the reaction ^{17}O(p,α)^{14}N is more efficient in the NACRE case by a factor of a few hundred, while the difference for the reaction ^{17}O(p,γ)^{18}F is a factor of ∼5. In the third panel, more importantly, we can see that the favorite channel of ^{17}O destruction switches from ^{17}O(p,α)^{14}N to ^{17}O(p,γ)^{18}F passing from the NACRE to the CF88 cross-sections.

This, in turn, has two important consequences:

- In the CF88 models we have a much larger production of the heaviest oxygen isotopes.
- In the NACRE case, the equilibrium abundance of ^{17}O is much lower, and the nucleosynthesis favors a return to ^{14}N rather than a production of ^{18}F: this explains the differences between the CNO abundances of the ejecta of the two sets of models which can be seen in Fig. 11.

Turning to heavier elements, we show in the four panels of Fig. 13 the abundances of ^{23}Na and ^{24}Mg of the ejecta of the different models, and the ratio of the magnesium isotopes, ^{25}Mg/^{24}Mg and ^{26}Mg/^{24}Mg. We note from the left-upper panel of Fig. 13 that sodium production can be achieved efficiently in the NACRE case, while it is not present in the CF88 models. This can be explained very simply on the basis of the cross-section of the reaction ^{22}Ne(p,γ)^{23}Na, which, in the range of temperatures relevant in this case, is lower in the CF88 case by at least a factor of ∼100, reaching a maximum difference of a factor of ∼2000 for $\log(T) = 7.8$.

In the two panels of Fig. 14 we compare the variation with mass of the ^{22}Ne and ^{23}Na surface abundances within two models of initial mass 5 $M_\odot$ calculated with the NACRE and CF88 nuclear cross sections. We see an early phase of sodium production and neon destruction during the first thermal pulses in the NACRE model, and a later increase of the sodium abundance due the dredging-up of ^{22}Ne, which is later converted to ^{23}Na. In the CF88 case the surface ^{22}Ne never decreases, and sodium is destroyed when the temperatures at the base of the external zone become large enough to efficiently activate the Ne–Na cycle.

The top and middle right panels of Fig. 12 show the ratio of the cross-sections corresponding to the two channels of sodium destruction (^{23}Na(p,γ)^{24}Mg and ^{23}Na(p,α)^{20}Ne) (always in terms of CF88/NACRE value) and the ratio $\sigma(^{23}\mathrm{Na(p,}\gamma)^{24}\mathrm{Mg})/\sigma(^{23}\mathrm{Na(p,}\alpha)^{20}\mathrm{Ne})$ in the two cases. In the NACRE case sodium is destroyed more easily, and the favorite channel is magnesium production in the relevant range of temperatures; this determines a larger ^{24}Mg equilibrium abundance, and explains the difference between the models which can be seen in the right-upper panel of Fig. 13.

Turning to the magnesium isotopic ratios, ^{25}Mg/^{24}Mg is similar in the two cases (see the left-lower panel of Fig. 13), while ^{26}Mg/^{24}Mg is lower in the CF88 models; the reason is that the rate of the reaction ^{26}Mg(p,γ)^{27}Al is a factor of ∼10 larger in the CF88 case, thus favouring ^{26}Mg destruction in favor of ^{27}Al production.

By comparing the AGB models calculated with the two sets of cross-sections we conclude that the physical behavior is essentially the same, because the rates of the reactions mostly contributing to the global energy release are barely changed. In terms of nucleosynthesis (and therefore of the average chemical content of the ejecta) we find important variations only for sodium and the heavier isotopes of oxygen. The former is not produced at all in the CF88 models (contrary to the NACRE case) due to the extremely low cross-section of the ^{22}Ne proton capture reaction; the equilibrium abundances of ^{17}O and ^{18}O are much lower in the NACRE case, because of the larger values of both the ^{17}O proton capture reactions.

5. The role of mass loss

The effects of mass loss on the evolution of AGB stars is well documented in the literature (Schönberner 1979): mass loss halts the increase of luminosity, and progressively peels off all the envelope, eventually leaving a central remnant which evolves as a white dwarf. It determines a general cooling of the structure, therefore reducing the intensity of HBB at the base of the external convective zone. Since the effects of mass loss become evident only when the mass of the envelope is considerably reduced, models with different mass loss rates will differ only in the terminal part of their evolution, while the general physical behavior during the first TPs is unchanged.

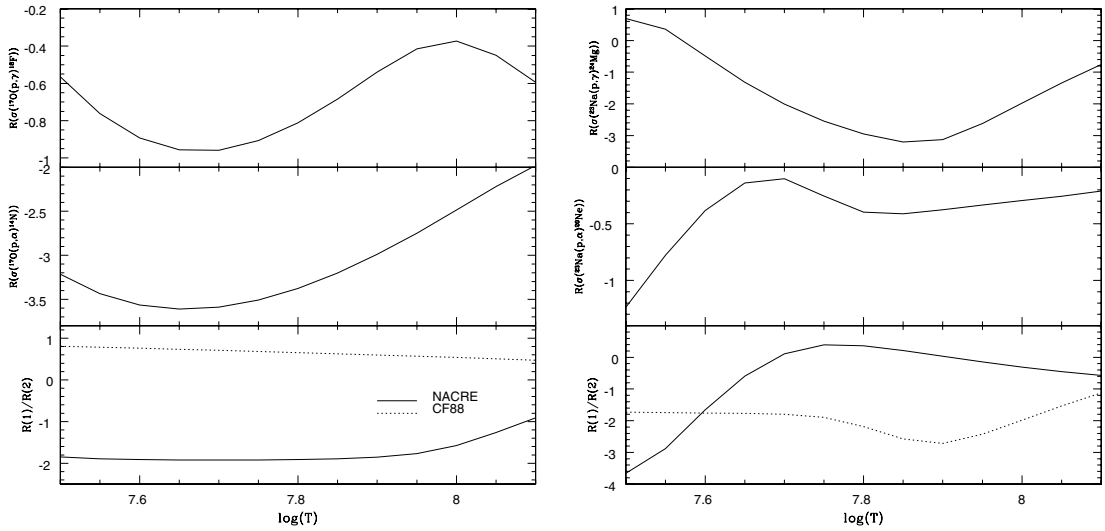

Fig. 12. *Left*: variation with temperature of the logarithm of the ratio between the CF88 and the NACRE cross section of the reaction ^{17}O(p,γ)^{18}F (*top*), ^{17}O(p,α)^{14}N (*middle*) and of the ratio $\sigma(^{17}\mathrm{O(p,}\gamma)^{18}\mathrm{F})/\ \sigma(^{17}\mathrm{O(p,}\alpha)^{14}\mathrm{N})$ (*bottom*). *Right*: the same as the left panel, but for reactions ^{23}Na(p,γ)^{24}Mg and ^{23}Na(p,α)^{20}Ne.

The NACRE and CF88 models presented in the previous sections were calculated with the parameter $\eta_{\rm R} = 0.02$, in Blöcker's formula. This choice is due to a previous calibration, made on the basis of a detailed comparison between the observed and the theoretical luminosity function of lithium rich AGB stars in the Magellanic Clouds (Ventura et al. 2000). For our models, a value of $0.01 \leq \eta_{\rm R} \leq 0.02$ for stars with initial mass in the range $3 \leq M/M_{\odot} \leq 4.5$ is able to reproduce the observed trend of surface lithium vs. luminosity which is observed in the Clouds.

We cannot completely rule out the possibility that the parameter $\eta_{\rm R}$ to be used during the AGB evolution might show a dependency on the metallicity (we recall that the models discussed in this paper have a metallicity which is a factor of 10 lower than the LMC stars) and on the stellar mass, or that the mass loss is heavily influenced by the environment. In order to test the level of uncertainty connected to the mass loss, we decided to explore the sensitivity of our results on changes in the value of $\eta_{\rm R}$, and we discuss it for for two representative examples of our stars.

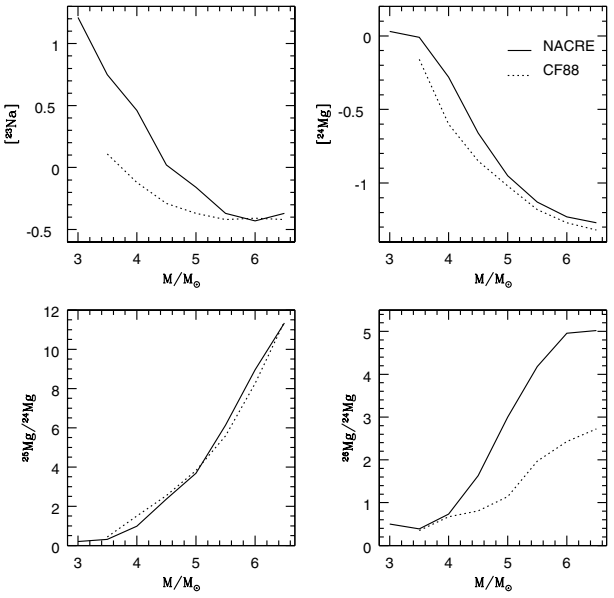

Fig. 13. Average chemical content of the ejecta of IMS models calculated with NACRE (solid) and CF88 (dotted) sets of nuclear cross-sections in terms of ^{23}Na and ^{24}Mg. The bottom panels show the isotopic ratios of magnesium.

5.1. Massive AGBs

We compare the standard model of initial mass 5 $M_{\odot}$ already presented in Sect. 3 (eta002 model) with two models of the same initial mass, computed by assuming, respectively, $\eta_{\rm R} = 0.1$ (eta010 model) and $\eta_{\rm R} = 0.2$ (eta020 model). Figure 15 shows the variation with time of the mass. Times have been set to 0 at the beginning of the AGB evolution. We see that the total duration of the AGB phase is strongly dependent on $\eta_{\rm R}$, ranging from $t_{\rm AGB} \sim 73\,000$ yr for the eta002 model down to ~27 000 yr in the eta020 case. The eta002 model reaches a maximum luminosity of 66 000 $L_{\odot}$ during the 20th interpulse period, while the eta010 and eta020 models achieve a maximum luminosity of, respectively, 50 000 $L_{\odot}$ (13th interpulse period), and 43 500 $L_{\odot}$ (10th interpulse period). In conjunction with the maximum luminosity, all the models also attain the largest temperature at the base of the external envelope. The maximum $T_{\rm bce}$ are: $T_{\rm bce} = 103 \times 10^6$ K (eta002), $T_{\rm bce} = 100 \times 10^6$ K (eta010) and $T_{\rm bce} = 98 \times 10^6$ K (eta020). These values are quite similar, especially when compared to the differences in the maximum values of luminosity reached by the three models. This is not surprising, as a main feature of the FST convective model is that, within the most massive AGBs, it leads to a very efficient HBB already during the first TPs: even a strong increase of mass loss cannot prevent the base of the external zone from becoming extremely hot. On the basis of these results, we may

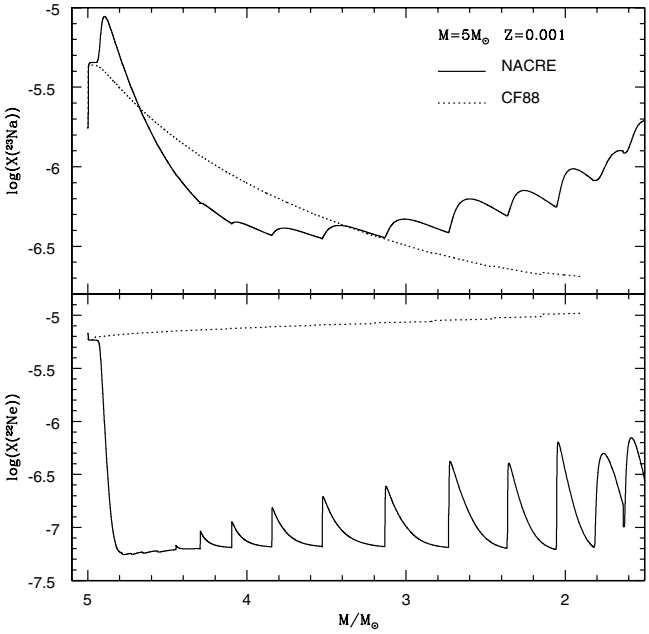

Fig. 14. The AGB evolution of the surface abundances of ^{23}Na (*top*) and ^{22}Ne (*bottom*) of two models with initial mass 5 $M_{\odot}$ calculated with the NACRE (solid) and CF88(dotted) nuclear cross-sections.

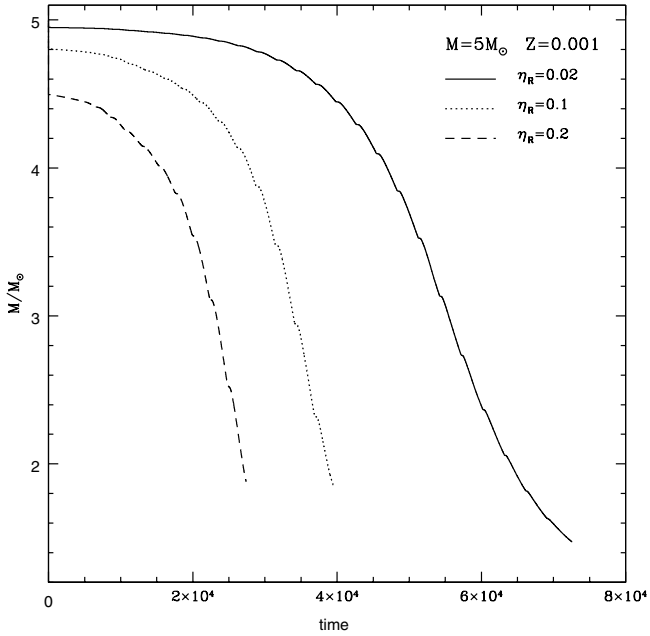

Fig. 15. Variation with time of the total mass of three models of initial mass 5 $M_{\odot}$ calculated with three different value of the parameter for mass loss, $\eta_{\rm R}$. Time has been set to 0 at the beginning of the AGB evolution.

expect deep nucleosynthesis to take place at the base of the external convective zone even in the eta020 model.

In the four panels of Fig. 16 we show the evolution of the surface CNO abundances for the three models, plus the variation of the total C+N+O abundance. For each of these elements we show both the variation with time and with mass. In the left-upper panel we show the variation of surface ^{12}C. In the top of this panel we see that the temporal evolution is very similar, with an early phase of destruction at the beginning of the AGB evolution followed by a later phase of production, when the temperatures at the base of the external zone are sufficient to allow the full CNO cycle to be activated, and the effects of the 3rd dredge-up become more evident. The only difference among the three models is that the AGB evolution is halted earlier for larger values of $\eta_{\rm R}$. Since for all the models the evolution stops when the carbon abundance was increasing, this acts in favor of a larger ^{12}C content of the ejecta for lower mass loss rates. In the lower part of this panel we see the evolution of ^{12}C with the stellar mass. The above effect is partly compensated by the fact that, for larger $\eta_{\rm R}$, the star loses a not negligible fraction of its mass when the carbon abundance was still unchanged, even before the early phase of destruction at the beginning of AGB. This is the reason why the average ^{12}C abundance of the ejecta of our models show a maximum difference of ∼0.1 dex, and is therefore consistent with the value [^{12}C] = −0.7 given in Sect. 3.

An analogous discussion can be made for nitrogen, as can be seen in the right-upper panel of Fig. 16. The surface ^{14}N increases in all cases, because nitrogen is created at the base of the external envelope due to HBB and, in the final part of the evolution, also due to the effects of the 3rd dredge-up. Again we note a strong similarity in the temporal evolution, the only difference being that in the large $\eta_{\rm R}$ models the ^{14}N content of the ejecta is expected to be lower because the AGB evolution is halted earlier. In reality, at odds with the ^{12}C case, we expect a larger nitrogen content of the ejecta of the eta002 model because this latter case loses less mass at the very beginning of the AGB evolution, when the ^{14}N abundance was still unchanged since the second dredge-up (see the lower part of the right-upper panel of Fig. 16). The ^{14}N average content of the ejecta is therefore more dependent on mass loss, ranging from [^{14}N] = 1.15 in the eta002 model, down to [^{14}N] = 0.83 in the eta020 model; the eta010 model, with [^{14}N] = 0.92, shows an intermediate behavior. The global spread of the [^{14}N] value varies at most by a factor of ∼2 if $\eta_{\rm R}$ varies by one order of magnitude.

As already pointed out, the temperatures at the base of the convective zone are sufficiently high to activate the full CNO cycle in all the models, so that in all cases we have a certain amount of ^{16}O depletion, as can be seen in the left-lower panel of Fig. 16. The trend of the ^{16}O average content of the ejected material for various $\eta_{\rm R}$ is straightforward:

- For larger values of $\eta_{\rm R}$ a consistent part of the envelope mass ($\Delta M \sim 1\ M_{\odot}$) is lost when the oxygen abundance is still unchanged.
- Since the temperature at the base of the envelope reached by the large $\eta_{\rm R}$ models is lower, in these cases ^{16}O is destroyed less heavily, and this leads to higher oxygen equilibrium abundances.

We thus find that a strong oxygen destruction is hardly found within the models with the largest mass loss rates. The [^{16}O] of the ejecta is more dependent than [^{14}N] on the assumed $\eta_{\rm R}$: we have [^{16}O] = −0.6 for the eta002 model, [^{16}O] = −0.3 in the $\eta_{\rm R}$ = 0.1 case, and [^{16}O] = −0.15 for $\eta_{\rm R}$ = 0.2.

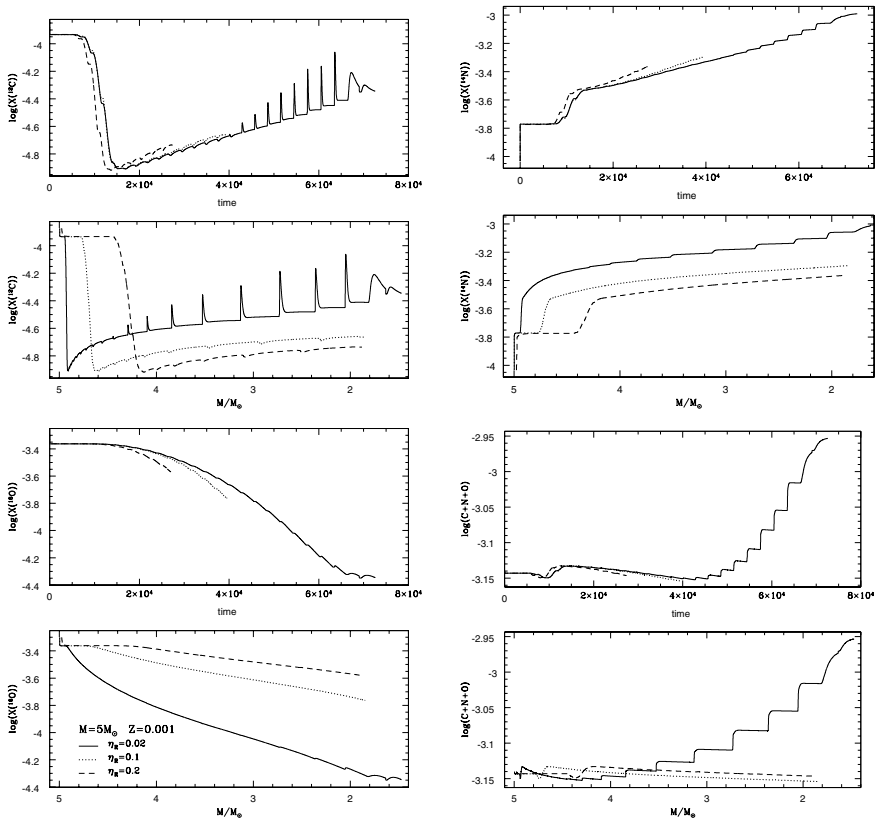

Fig. 16. Variation with time and total mass of the CNO surface abundances of the same models presented in Fig. 15. The right-lower panel shows the total C+N+O abundance. The abundances are given in mass fraction.

In the right-bottom panel of Fig. 16 we show the total C+N+O abundance. In the eta010 and eta020 models the sum of the CNO abundances is constant, because mass is lost so rapidly that the effects of the 3rd dredge-up are negligible. In the eta002 model, during the last TPs, carbon is efficiently dredged-up, and is later converted to ^{14}N by HBB; however, the total increase of the C+N+O is within ∼0.2 dex. We may therefore conclude that within the FST framework the most massive AGB models show surface C+N+O abundances that are constant within a factor of ∼2, independently of mass loss.

Turning to heavier nuclei, we focus our attention on sodium. Figure 17 shows the variation of the surface sodium abundance as a function of time (top panel) and mass (bottom). An early phase of production, due to proton capture by ^{22}Ne nuclei, is followed by a phase of sodium destruction when the temperatures at the base of the outer convective zone become large enough that sodium is destroyed by proton capture. A larger mass loss rate acts in favor of larger sodium yield because a large fraction of the stellar mass is lost when sodium is produced, and also because the evolution is halted when the surface sodium has not yet been completely destroyed (bottom panel).

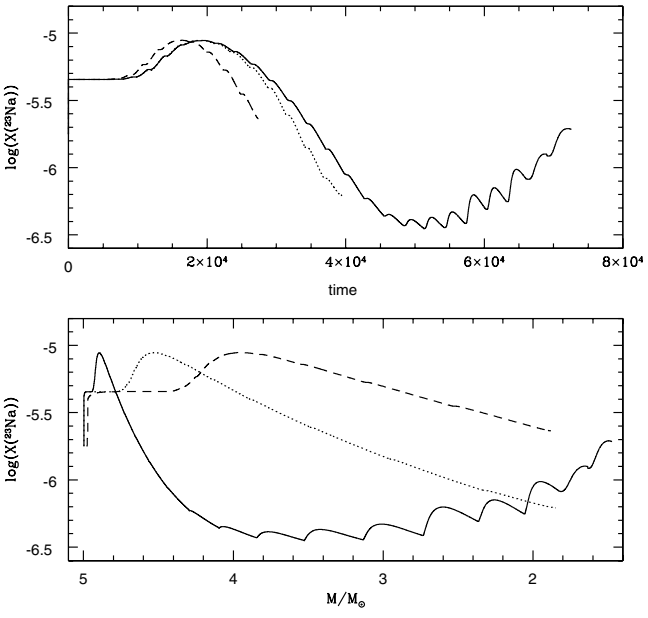

Fig. 17. AGB evolution of the surface abundances of ^{23}Na (*top*) and ^{22}Ne (*bottom*) of the same models presented in Fig. 15.

Actually, sodium turns out to be the element most sensitive to variations of the mass loss rate. A larger η_R changes completely the situation, in the sense that now we expect the mass expelled by massive AGBs to be sodium rich (with respect to the initial mass fraction) rather than sodium poor. [^{23}Na] linearly increases with η_R, while a positive sodium yield is not possible at 5 $M_\odot$ with the standard $\eta_R = 0.02$ value. The oxygen yield shows a similar behavior, though in this case the convection is so efficient that [^{16}O] is negative in all cases. A simultaneous sodium production and oxygen depletion in the

chemistry of the ejecta, in agreement with the observed anti correlation, is possible only for $\eta_R \sim 0.1$.

We find that ^{24}Mg is depleted in all cases, but the final abundance is a factor of ∼500 lower in the eta002 case, while it is just a factor of 2 lower in the eta020 model. The ^{24}Mg abundance of the ejecta is a factor of ∼10 lower than the initial value for the eta002 model, while it is lower by only ∼0.1 dex for $\eta_R = 0.20$.

The average content of ^{25}Mg is not strongly dependent on the mass loss rate, because it reaches a maximum value and then declines as ^{24}Mg is destroyed; in reality, in the eta010 and eta020 models the evolution is completed when the ^{25}Mg is almost at its maximum value. The net result is that within ∼0.1 dex we find $[^{25}\mathrm{Mg}] = 0.5$ for all the models. The situation is different for the heaviest isotope, because the surface ^{26}Mg increases for the whole evolution. In this case a larger mass loss rate leads to a lower final abundance, so that the yield is lower. For the eta002 model we find $[^{26}\mathrm{Mg}] = 0.35$, while $[^{26}\mathrm{Mg}] = 0.15$ in the $\eta_R = 0.01$ case. The average ^{26}Mg content of the eta020 model is practically unchanged with respect to the initial value.

In terms of isotopic ratios, lower values of both ^{25}Mg/^{24}Mg and ^{26}Mg/^{24}Mg are expected for larger mass loss rates, because in that case we have a lower depletion of ^{24}Mg. In agreement with that, we find isotopic ratios ∼3 for $\eta_R = 0.02$, ∼1 for $\eta_R = 0.1$ and ∼.4 for $\eta_R = 0.2$, the ^{25}Mg/^{24}Mg ratio being always slightly larger than the ^{26}Mg/^{24}Mg.

5.2. The 4 $M_\odot$ model

The situation is a bit more complex for lower masses, because in that case the temperature reached by the base of the outer convective zone never exceeds $\sim 10^8$ K, therefore they achieve only in a later phase of their AGB evolution the conditions necessary to trigger a deep nucleosynthesis within the convective envelope. In these cases, at odds with the most massive models, we expect that a stronger mass loss, triggering an earlier cooling of the structure, may prevent some reactions from occurring at all.

We therefore calculated a model with initial mass $M = 4\ M_\odot$ with a parameter for mass loss $\eta_R = 0.10$ (eta010 model), and we compare it with the model with the same initial mass calculated with $\eta_R = 0.02$, presented in Sect. 3. The total duration of the AGB phase for the eta010 model is shorter, as expected: the total mass of the star reduces to ∼1.4 $M_\odot$ within $t_{AGB} \sim 87\,000$ yr, to be compared to $t_{AGB} \sim 150\,000$ yr of the eta002 model.

In Fig. 18 we compare the variation with time of the luminosity and of the temperature at the base of the envelope of the two models, as a function of the AGB time. We see from the top panel that there is a difference of ∼0.2 dex between the maximum value of the luminosity reached by the two models, while, in terms of temperature, the base of the convective zone of the eta002 model achieves a maximum value of $T_{bce} = 95 \times 10^6$ K, to be compared to the maximum temperature $T_{bce} = 88 \times 10^6$ K reached in the $\eta_R = 0.10$ case. In terms of the chemical content of the ejecta, we may repeat for ^{12}C and ^{14}N the same

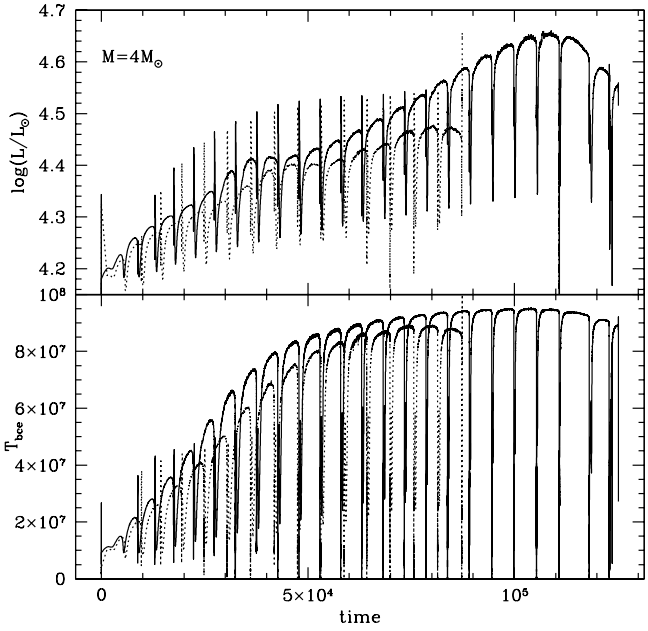

Fig. 18. The evolution of luminosity (*top*) and temperature at the base of the envelope *(bottom)* of two models with initial mass 4 $M_\odot$ calculated with two values of the parameter entering Blöcker (1995) prescription for mass loss: $\eta_R = 0.02$ (solid track) and $\eta_R = 0.1$ (dotted).

discussion as for the 5 $M_\odot$ model, because the temperatures in this case, though lower, are still sufficient to favor an early phase of ^{12}C destruction followed by a later phase of production, and a progressive increase of the surface ^{14}N abundance due both to HBB and to the effects of the 3rd dredge-up. Thus, the ^{12}C abundance of the ejecta is almost the same for both models, while the ^{14}N abundance is lower in the eta010 model by a factor of ∼2.

The different values of the temperatures reached at the base of the outer convective zone in the two models lead to a different degree of oxygen depletion at the base of the envelope, as can be seen in the two panels of Fig. 19, where we show the variation of the surface ^{16}O with time (top panel) and mass (bottom). We see that both models start to deplete oxygen after ∼40 000 yr, but the depletion is made difficult in the eta010 model by the lower temperatures, so that the final abundance is only ∼0.15 dex lower than the ^{16}O present in the envelope at the beginning of the TPs phase. In the eta002 model a stronger depletion is achieved. The average oxygen content of the ejecta is $[^{16}\mathrm{O}] = -0.4$ in the eta002 model, while it is $[^{16}\mathrm{O}] = -0.1$ for $\eta_R = 0.1$. Even for the $M = 4\ M_\odot$ model we find that the C+N+O abundance is constant within a factor of ∼2 for the whole evolution, the eta002 model showing the largest increase due to the higher number of 3rd dredge-up episodes.

The situation concerning sodium is more complex. The eta002 model, after the initial phase of production, destroys sodium more efficiently due to the larger temperatures reached; yet, the evolution is so long that some sodium is dredged-up later on; as a consequence, the sodium content of the ejecta is almost the same in the two cases, i.e. $[^{23}\mathrm{Na}] = 0.5$. The less massive models are therefore efficient sodium producers,

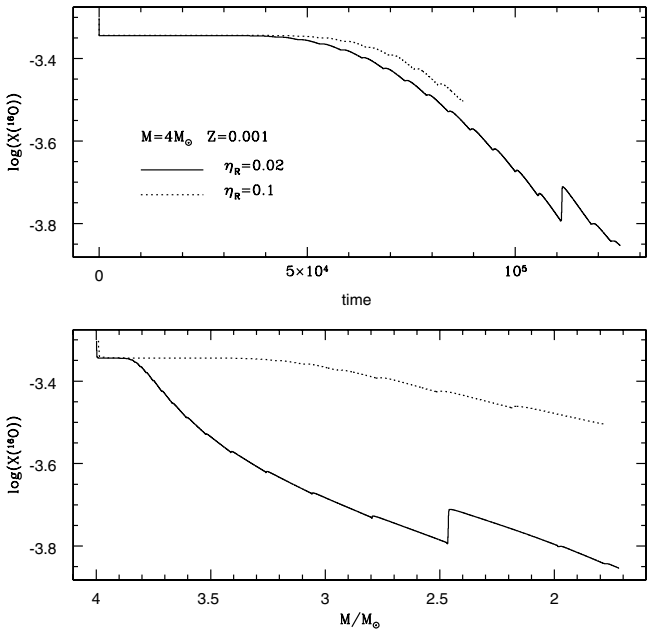

Fig. 19. Comparison between the depletion of surface oxygen within two models with initial mass 4 $M_{\odot}$ calculated with two different values of $\eta_{\rm R}$.

independently of the mass loss rate adopted. In terms of the oxygen-sodium anti-correlation, the eta002 model in this case is consistent with simultaneous oxygen depletion and sodium production, while only a poor oxygen depletion is expected for higher mass loss rates.

For magnesium, the situation is very different to the 5 $M_{\odot}$ case. The temperatures here are not sufficiently high to favor an efficient magnesium destruction, so that even in the eta002 model ^{24}Mg is reduced by only a factor of ∼2. For $\eta_{\rm R}$ = 0.1 the surface ^{24}Mg is almost unchanged. Even for the heavier isotopes the production is much lower than in the 5 $M_{\odot}$ model. In terms of the isotopic ratios, we find ^{25}Mg/^{24}Mg ∼ 0.9 and 0.2, respectively, for $\eta_{\rm R}$ = 0.02 and $\eta_{\rm R}$ = 0.1, while ^{26}Mg/^{24}Mg is 0.7 for $\eta_{\rm R}$ = 0.02 and 0.2 for $\eta_{\rm R}$ = 0.1.

We may therefore summarize the influence of mass loss on the AGB models as follows:

1. The carbon content of the ejecta is almost independent of mass loss, while the nitrogen abundance may vary by a factor of ∼2, lower $\eta_{\rm R}$ models showing greater enhancement. This holds for all the masses calculated, because at least the CN cycle is always operating.
2. The oxygen abundance of the ejecta proves to be more sensitive to mass loss; a lower $\eta_{\rm R}$ favors larger oxygen depletion. For all the masses considered we achieve oxygen depletion for $\eta_{\rm R}$ = 0.02, while a poor depletion is expected for larger values of $\eta_{\rm R}$, particularly for the lowest masses.
3. The C+N+O sum is in all cases constant within a factor of ∼2, independently of mass and mass loss.
4. Larger $\eta_{\rm R}$ favor sodium production in the more massive models, because in that case the AGB evolution is halted when the surface sodium has not yet been destroyed. The less massive models are efficient sodium producers, independently of the mass loss rate.
5. The isotopic magnesium isotopes stay below unity independently of mass loss for the less massive models. For higher masses we have a steeper dependence on $\eta_{\rm R}$: we find ^{25}Mg/^{24}Mg ∼ ^{26}Mg/^{24}Mg ∼ 3 for $\eta_{\rm R}$ = 0.02, down to ^{25}Mg/^{24}Mg ∼ ^{26}Mg/^{24}Mg ∼ 0.4 for $\eta_{\rm R}$ = 0.2.

6. What implications for the self-pollution scenario?

There is still a strong debate concerning the role that AGBs may have played in the pollution of the interstellar medium of GCs: Fig. 7 shows that we are far from being able to falsify the hypothesis that the chemical content of their ejecta may account for the chemical anomalies observed in GC stars (Denissenkov & Herwig 2003; Fenner et al. 2004; Ventura et al. 2002; Paper I).

Within the MLT framework for the treatment of convection the most recent work by Fenner et al. (2004) shows that it is hardly possible to reconcile the theoretical findings with the observational scenario, because the expected chemical content of the ejecta show a largely increased value of the global C+N+O abundance, a very poor oxygen depletion, and an extremely large sodium production. These results are all in contrast with the observational evidence. Their findings were confirmed by our AGB models calculated with the MLT convection, presented and extensively discussed in Paper I.

If the FST model is used, due to the higher temperatures reached at the bottom of the external envelope, we find on the contrary that the C+N+O is always constant within a factor of ∼2, in agreement with the results of Ivans et al. (1999). Also, oxygen depletion is easily achieved in all models more massive than 3 $M_{\odot}$.

The FST models in the range 3.5−4.5 $M_{\odot}$ with a mass loss rate in agreement with the calibration given in Ventura et al. (2000) pollute the interstellar medium with material having a chemistry qualitatively in agreement with the chemical anomalies observed, that is:

- The C+N+O sum is almost constant.
- Oxygen and sodium are anticorrelated, in qualitative agreement with the observed trend. From a quantitative point of view a larger sodium content, coupled to an even stronger oxygen depletion would be necessary to match the observational evidence.
- The magnesium isotopic ratios are well below unity, but the ^{26}Mg/^{24}Mg ratio is larger than the ^{25}Mg/^{24}Mg, contrary to observations (Yong et al. 2003). In addition, the magnesium vs. aluminum anti-correlation is not reproduced.

In the most massive models, on the contrary, the temperatures are so high that sodium, after an early phase of production at the beginning of the AGB phase, is destroyed; with the standard $\eta_{\rm R}$ = 0.02 value for the mass loss rate parameter we expect to have a negative [Na/Fe] and a correlation between sodium and oxygen. One further problem in this case would be the extremely high values of the magnesium isotopic ratios,

which cluster around ∼3, due to strong ^{24}Mg burning. If a larger mass loss rate is adopted, we expect poor oxygen depletion and sodium destruction, which would be more consistent with the observations. The magnesium isotopic ratios would be in this case below unity, which is also in better agreement with the observed abundances (Yong et al. 2003).

The CF88 models share almost the same properties of the NACRE models, with the only difference of sodium, which cannot be produced in this latter case, because of the extremely low values of the ^{22}Ne proton capture reaction cross-sections.

7. Conclusions

We present AGB models of intermediate mass in the range $3\ M_{\odot} \leq M \leq 6.5\ M_{\odot}$ with metallicity $Z = 0.001$.

This work, together with the results of Paper I, explores the role of some parameters of AGB evolution and shows that it is affected by so many uncertainties that it is still implausible to use the results of a unique set of AGB computations to falsify the self-enrichment scenario for globular cluster stars. Nevertheless, these results show trends in the yields that are different from those of other researchers, and may be relevant for a solution of the self-enrichment problem. In particular, contrary to several recent AGB computations, and by the use of the FST model, we find that convection at the base of the external zone during the quiescent phase of CNO burning is so efficient as to lead to extremely high temperatures ($T_{\rm bce} \sim 10^8$ K), sufficient to trigger strong HBB. We find that oxygen is depleted in all cases, with the only exception of the 3 $M_{\odot}$ model.

Our main findings are the following:

1. The physical behavior of the models turns out to be independent of the nuclear cross-sections used, the results obtained with the NACRE rates being very similar to CF88: this is due to the fact that the reactions most contributing to the global energy release, i.e. proton capture by carbon and nitrogen nuclei, are the same in the two cases.
2. One strong prediction, which holds independently of mass, is that the total C+N+O abundance of the ejecta is almost constant, at odds with previous investigations.
3. Sodium is produced within the NACRE models with $M < 4.5\ M_{\odot}$, while it is destroyed in the more massive stars, due to an efficient action of the Ne–Na cycle. In the CF88 models sodium is systematically destroyed, because of the extremely low values of the ^{22}Ne proton capture reaction.
4. In terms of magnesium isotopes, the ^{25}Mg/^{24}Mg and ^{26}Mg/^{24}Mg ratios are well below unity in the models with $M < 4.5\ M_{\odot}$, while they reach values approaching ∼10 for $M > 5\ M_{\odot}$, due to strong ^{24}Mg burning.
5. Mass loss influences the global duration of the AGB life; it also determines a general cooling of the structure before some nuclear reactions can be efficiently activated, therefore changing the average chemical content of the ejecta. With very strong mass loss, the HBB nucleosynthesis has no time to be completely established. This affects mainly the oxygen and sodium yields, while it leaves almost unaltered the lithium yield. In the most massive models a stronger mass loss rate (with respect to the standard value adopted, calibrated on slightly less massive models to reproduce the lithium-rich stars luminosity function in the LMC) might lead to ejecta that are sodium rich, and that show low magnesium isotopic ratios; there are two factors behind such findings:
   - i) Massive AGBs achieve large luminosities already during the first TPs; if mass loss is increased during these phases, we have a larger ejection of material that is still sodium rich and not extremely ^{24}Mg depleted.
   - ii) As a consequence of the reduction of the mass of the envelope, the evolution is halted earlier, before strong sodium and ^{24}Mg depletion can take place.

For models with masses $M \leq 4.5\ M_{\odot}$ the ejecta are sodium rich and with low magnesium isotopic ratios, with the only difference that, for larger values of $\eta_{\rm R}$, oxygen is scarcely depleted, as the increase of the temperature at the base of the external envelope is halted before it reaches values sufficiently high to activate efficiently the full CNO cycle.

These models show that the predictive power of AGB models is still undermined by many uncertainties. The parameter space, however, has not yet been fully explored (e.g. the role of extra-mixing at the bottom of the envelope) and for this reason we should not discard the hypothesis that massive AGB stars are responsible for the chemical anomalies observed in GC stars.

References

Angulo, C., Arnould, M., Rayet, M., et al. 1999, Nucl. Phys. A, 656, 3
Arnould, M., Goriely, S., & Jorissen, A. 1999, A&A, 347, 572
Blöcker, T. 1995, A&A, 297, 727
Blöcker, T., & Schönberner, D. 1991, A&A, 244, L43
Böhm-Vitense, E. 1958, Z. Astroph., 46, 108
Bonifacio, P., Pasquini, L., Spite, F., et al. 2002, A&A, 390, 91
Canuto, V. M., & Mazzitelli, I. 1991, ApJ, 370, 295
Canuto, V. M., Goldman, I., & Mazzitelli, I. 1996, ApJ, 473, 570
Carretta, E. 2003, Mem. S.A.It. Suppl., 3, 90
Carretta, E., Bragaglia, A., Cacciari, C., & Rossetti, E. 2003, A&A, 410, 143
Caughlan, G. R., & Fowler, W. A. 1988, At. Data Nucl. Tab., 40, 283
Cloutman, L., & Eoll, J. G. 1976, ApJ, 206, 548
Cloutman, L., & Whitaker, R. W. 1980, ApJ, 237, 900
Cohen, J. G., & Meléndez, J. 2005, AJ, 129, 303
Cohen, J. G., Briley, M. M., & Stetson, P. B. 2002, AJ, 123, 2525
D'Antona, F., & Mazzitelli, I. 1996, ApJ, 470, 1093
D'Antona, F., Gratton, R., & Chieffi, A. 1983, Mem. S.A.It., 54, 173
D'Antona, F., Caloi, V., Montalban, J., Ventura, P., & Gratton, R. 2002, A&A, 395, 69
Denissenkov, P., & Herwig, F. 2003, ApJ, 590, L99
Denissenkov, P., & Weiss, A. 2004, ApJ, 603, 119
Fenner, Y., Campbell, S., Karakas, A. I., Lattanzio, J. C., & Gibson, B. K. 2004, MNRAS, 353, 789
Gratton, R., Bonifacio, P., Bragaglia, A., et al. 2001, A&A, 369, 87
Gratton, R., Sneden, C., & Carretta, E. 2004, ARA&A, 42, 385
Grundahl, F., Briley, M., Nissen, P. E., & Feltzing, S. 2002, A&A, 385, L14
Herwig, F. 2000, A&A, 360, 952

Herwig, F. 2004, A&A, 605, 425
Herwig, F., Blöcker, T., & Schönberner, D. 1997, A&A, 324, L81
Iben, I. J. 1975, ApJ, 196, 525
Iben, I. J. 1976, ApJ, 208, 165
Ivans, I. I., Sneden, C., Kraft, R. P., et al. 1999, AJ, 118, 1273
Lattanzio, C. L., & Karakas, A. I. 2001, M.S.A.It., 72, 255
Mazzitelli, I., D'Antona, F., & Ventura, P. 1999, A&A, 348, 846
Pilachowski, C. A. 1988, ApJ, 326, L57
Ramirez, S., & Cohen, J. G. 2002, AJ, 123, 3277
Ramirez, S., & Cohen, J. G. 2003, AJ, 125, 224
Renzini, A., & Voli, M. 1981, A&A, 94, 175
Sackmann, J., & Boothroyd, A. I. 1991, ApJ, 366, 529
Schönberner, D. 1979, A&A, 79, 108
Schwarzschild, M., & Harm, R. 1965, ApJ, 142, 855
Schwarzschild, M., & Harm, R. 1967, A&A, 145, 486
Smith, G. H., Shetrone, M. D., Bell, R. A., Churchill, C. W., & Briley, M. M. 1996, AJ, 112, 1511
Sneden, C., Kraft, R. P., Guhathakurta, P., Peterson, R. C., & Fulbright, J. P. 2004, AJ, 127, 2162
Ventura, P., & Castellani, M. 2005, A&A, 430, 1035
Ventura, P., & D'Antona, F. 2005, A&A, 431, 279
Ventura, P., Zeppieri, A., D'Antona, F., & Mazzitelli, I. 1998, A&A, 334, 953
Ventura, P., D'Antona, F., & Mazzitelli, I. 2000, A&A, 363, 605
Ventura, P., D'Antona, F., Mazzitelli, I., & Gratton, R. 2001, ApJ, 550, L65
Ventura, P., D'Antona, F., & Mazzitelli, I. 2002, A&A, 393, 215
Vitense, E. 1953, Zs.Ap., 32, 135
Yong, D., Grundahl, F., Nissen, P. E., & Shetrone, M. D. 2003, A&A, 402, 985